Estimation of ship size from satellite optical image using elliptic characteristics of ship periphery

Jae-Jin Park, Kyung-Ae Park, Pierre-Yves Foucher, Moonjin Lee, Sangwoo Oh

Estimation of ship size from satellite optical image using elliptic characteristics of ship periphery

Jae-Jin Park[a], Kyung-Ae Park[b], P-Y Foucher[c], Moonjin Lee[d] and Sangwoo Oh[d]

[a]Department of Science Education, Seoul National University, Seoul, Korea; [b]Department of Earth Science Education/Research Institute of Oceanography, Seoul National University, Seoul, Korea; [c]Theoretical and Applied Optics Department, Office National d'Etudes et Recherches Aérospatiales, Toulouse, France; [d]Maritime Safety and Environmental Research Division, Korea Research Institute of Ships and Ocean Engineering, Daejeon, Korea

ABSTRACT

As the volume of marine transportation increases, it becomes increasingly important to monitor ships for efficient coastal mon-itoring and management. To this end, high-resolution satellite images can be utilized to surveil oceanic environments synoptically. In this study, high-resolution optical satellite image was used to detect ships and estimate the size of each ship in the Korean coastal region. All the pixels in an image were first classified into ship, ship shadow, wake, sea, and land by applying a maximum likelihood classifier. The positions corresponding to the boundary of the ship were obtained from the magnitude of the 2-dimensional gradient on the classified ship pixels, and then the length and width of the ship were estimated by applying an ellipse fitting method to the ship periphery. This method resulted, in slight overestimations of the sizes of the ships. In order to improve the accuracy of the estimated ship sizes, a correction formula was developed by inves-tigating the errors of the estimated values and their potential relationships to the variables representing the spatial shape of the vessels, such as eccentricity, kurtosis. Applying the suggested for-mulation for ship size estimation improved accuracy by 54.41%compared to the estimated sizes obtained through ellipse fitting. We anticipate that our method of estimating the lengths of the vessels will contribute to identifying missing ships using high-resolution satellite images.

1. Introduction

Marine trade and traffic volume in coastal regions have been consistently increasing over time. As the scale of marine affairs and various types of coastal disasters have increased, there has been a proportional increase in efforts to monitor vessels and manage marine resources (Kanjir, Greidanus, and Oštir 2018). Marine accidents such as collisions, fires, explosions, and sinking have also been increasing around the Korean peninsula over time (Kim, Na, and Ha 2011). In particular, human-made disasters such as the Hebei Spirit oil spill accident in Taean in December 2007 and the oil spill in Yeosu in January 2014 caused

considerable economic losses due to the leakage of large amounts of crude oil (Kim et al. 2010, 2015; Lee et al. 2016).

In the event of a ship accident, it is important to locate the missing ship promptly to minimize potential damages. The search for missing ships can be carried out by other ships, but this requires considerable time and cost, especially at offshore regions far from the coastline as well as in the open ocean. As the areas of marine activity have expanded through time, real-time monitoring using ships has becomes more difficult. Recently, illegal fishing has emerged as a serious problem internationally. It is very difficult to identify illegal fishing boats that enter a foreign country's sea territory without official sanction. The locations of ships can be obtained using the Automatic Identification System (AIS) installed on board, thus improving maritime safety, efficiency of navigation, and the protection of marine environments (IALA 2003). AIS data is widely used to detect missing ships or those sunk due to collision with rocks or other ships, via information sources for maritime traffic monitoring (position, identification, course, speed, etc.) (Eriksen et al. 2006; Zhao et al. 2014; Zhang et al. 2015).

However, most ships intentionally turn off their AIS to hide their locations. According to statistical surveys, the number of officially sanctioned fishing boats amounted to 1,700 in 2012 (Shin 2013). In contrast, the number of illegal foreign ships amounted to the extremely high number of 10,000 off the coast of Korea. Such illegal and reckless fishing have resulted in overfishing in the seas around the Korean Peninsula and significantly damaged the local fishery economy by degrading the surrounding marine ecosystem.

On the other hand, satellite remote sensing enables near real-time monitoring and can effectively provide additional information over a wide area. Ship detection can be accomplished via optical, Synthetic Aperture Radar (SAR), and hyperspectral sensor satellites. Optical remote sensing is regarded as one of the most useful ship detection techniques in various field of works such as marine traffic surveillance, marine rescue, and fishery management, although the ships are difficult to be observed from optical satellite images under cloudy weather condition (Scales and Swanson 1984; Jalkanen et al. 2009; Shi et al. 2014). Application studies have extensively used high-resolution optical images from SPOT-5, WorldView, Sentinel-2, and Gaofen with revisit periods of $3 - 5$ days to detect ships (Corbane et al. 2010; Qi et al. 2015; Kanjir 2019). Kanjir, Greidanus, and Oštir (2018) reviewed 119 papers on optical ship detection and classified the methods of detection into eight categories: the threshold classification method is based on a histogram algorithm (Corbane, Marre, and Petit 2008); other detection methods are based on image salience (Bi et al. 2012), shape and texture information of the ship (Zhu et al. 2010; Liu et al. 2014), statistical analysis including Principal Component Analysis (PCA) and Bayesian decision theory (Wu et al. 2009; Proia and Pagé 2010), and the transformation domain (Xu et al. 2014).

Additionally, there are anomaly detection methods based on Intensity Discrimination Degree (IDD) or Reed-Xiaoli algorithms (Shi et al. 2014; Yang et al. 2014), and computer vision methods such as Haar-like features (Mattyus 2013). Finally, there are ship detection method using neural networks or machine learning based on the crust patterns of the human brain (Tang et al. 2015; Yao et al. 2016). The actual ships are ultimately distinguished by utilizing the geometrical features such as the length and width, the ratio between the two, and their compactness (Liu et al. 2014; Yang et al. 2014; Heiselberg 2016). The Maximum-Likelihood Classifier (MLC) method was also used to detect ships from satellite images (Park et al. 2018).

Most studies on ship detection have focused on how many ships are to be detected rather than the size of a ship. In this study, our analyses have six objectives: 1) to classify all objects in optical images into five classes, namely, ship, shadow, wake, sea, and land; 2) to validate the accuracy of the ship location by matching the AIS data; 3) to extract the geographical location information of ship boundary pixels by a using 2-dimensional gradient; 4) to estimate the ship length and width by applying ellipse least squares fitting; 5) to estimate the accuracy of estimated ship sizes and errors; and 6) finally to develop an algorithm to estimate the ship size.

2. Data and methods

2.1. Satellite data and study area

The satellite optical image used in the study was observed by the Korea Multi-Purpose SATellite-2/3 (KOMPSAT-2/3), a multipurpose utility satellite launched by the Korea Aerospace Research Institute (KARI) on 28 July 2006 and 17 May 2012, respectively. The KOMPSAT-2 includes one Panchromatic (PAN) image with a spatial resolution of 1 m and four Multi Spectral (MS) images with a spatial resolution of 4 m and a revisit period of 5.5 days. On the other hand, the KOMPSAT-3, with an orbit period of 1.4 days, has a much higher resolution of 0.7 m and 2.8 m in spatial resolution for PAN and MS, respectively. The satellite has a footprint with a spatial coverage of 15 km × 15 km. Details of satellite specifications are summarized in Table 1. The detectable length of a ship is expected to be slightly longer than three times the pixel resolution of a satellite image, due to the spatial resolution of existing satellite imagery.

The KOMPSAT-2 image, captured at 01:25 UTC on 12 January 2013 and at 02:02 UTC on 15 March 2016, encompassed the study area consisting of the Gwangyang Bay at the southern coast of the Korean peninsula (Figure 1(b, c)). The KOMPSAT-3 image observed at 04:38 UTC on 7 September 2014 was also selected (Figure 1(d)). In order to detect ships located at sea, we removed the land pixels in the image using the Digital Elevation Model (DEM) operating on data with a resolution of 30 m × 30 m provided by the National Aeronautics and Space Administration (NASA) Shuttle Radar Topography Mission (SRTM). Since the coastlines of the Korean peninsula, especially in the study region, are so complicated and artificially change frequently, the DEM data failed to eliminate the land pixels completely. An additional procedure was required to successfully mask the pixels corresponding to land. As a result, pixels with a digital number (DN) greater than 45 in the near infrared channel were considered as land and removed following the procedure (Lee et al. 2016).

Table 1. Information on KOMPSAT-2/3 images including spectral ranges and spatial resolutions of panchromatic and multispectral images.

Satellite		KOMPSAT-2	KOMPSAT-3
Spectral band (nm)	Panchromatic	500 – 900	
	Multi spectral 1	450 – 520	
	Multi spectral 2	520 – 600	
	Multi spectral 3	630 – 690	
	Multi spectral 4	760 – 900	
Ground resolution (m)	Panchromatic	1	0.7
	Multi spectral 1 – 4	4	2.8

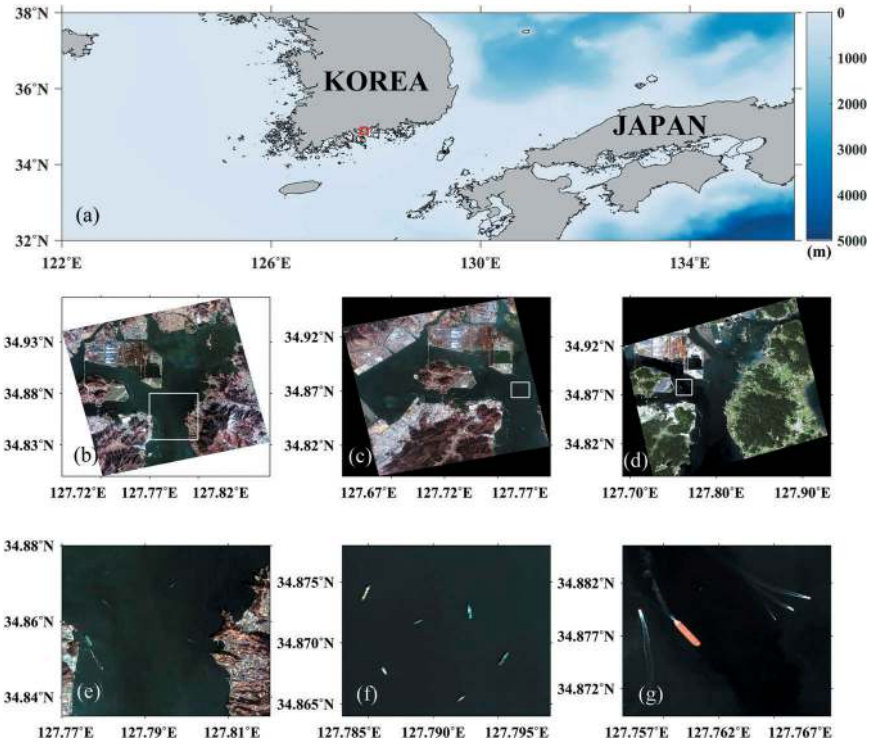

Figure 1. (a) Study area at the southern coast of the Korean peninsula, marked in a red box, (b) an RGB composite image of KOMPSAT-2 data at 01:25 UTC on 12 January 2013, (c) at 02:02 UTC on 15 March 2016, (d) and KOMPSAT-3 data at 04:38 UTC on 7 September 2014 and (e)–(g) an enlarged portion of the image of (b)–(d) (Park et al. 2018).

Figure 2 shows the spatial distributions of DN in the blue, green, red, and near infrared channels, with values ranging from 0 to 255. In all channels, the ship pixels have higher values than the sea pixels, and in particular, the two ships moored on the left lower part of the figure show relatively high values greater than 100. In contrast, the sea pixel present low values at long-wavelength channels such as the red and the near infrared channels (Figure 2(c, d)), compared to the other shorter wavelength channels in the blue and green bands (Figure 2(a, b)).

2.2. AIS data

To verify the geolocation of the ships detected using our vessel detection algorithm, we collected AIS information from the General Information Centre on Maritime Safety and Security (GICOMS), Ministry of Oceans and Fisheries, Korea. The AIS data includes ship location information in the study area, including time information within five minutes before and after the observation time of satellite images.

In addition, we collected information on ship in/out port provided by the Yeosu Gwangyang Port Corporation (https://www.ygpa.or.kr) and thirty cross sections of various types of ships were also obtained from searching the website of the ship manufacturer (https://shipdh.com). Such information of ship size and shape were utilized to estimate

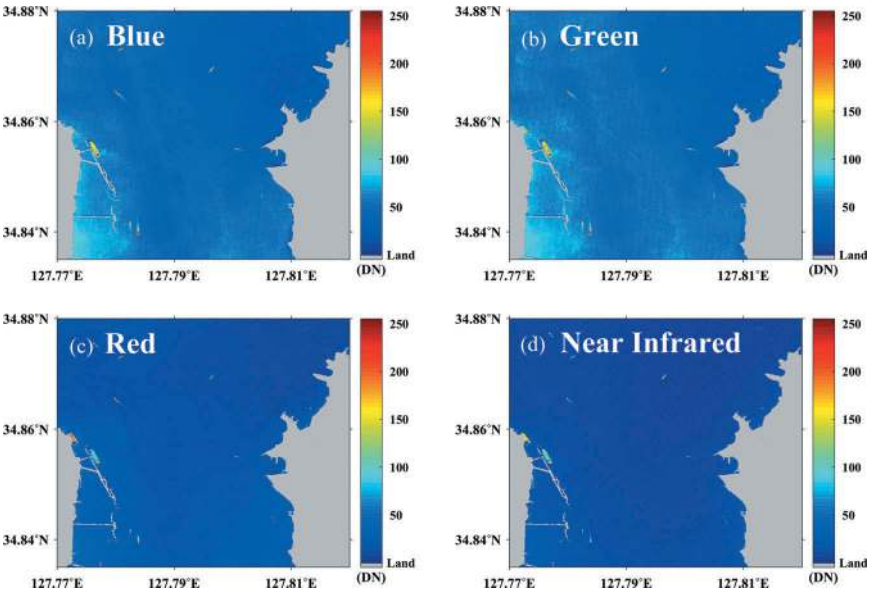

Figure 2. Spatial distribution of the digital number (DN) at each band of KOMPSAT-2 data at 01:25 UTC on 12 January 2013 corresponding to (a) blue, (b) green, (c) red, and (d) near-infrared spectral ranges.

the length and width of the ships in the study region and validate the analytical results from the algorithms developed in this study.

2.3. Image classification method

The MLC method assumes that all classes corresponding to each band follow a normal distribution, and the pre-classified classes can be expressed as a probability density function using mean and standard deviation (Richards and Jia 1999). This is a parametric classification method that takes into account the variance-covariance of each class (ERDAS 1999).

Figure 3(a) shows the distribution of the Gaussian probability density function in the red and green channels for the four classes of ship, wake, sea, and shadow. The four channels have DN values between 0 and 255, of which the ship pixels have the largest DN values with a wide spectral range. Figure 3(b) shows the contours of the 2-dimensional elliptic probability values for each class on the space domain consisting of red and green bands. The ship pixels have DN values greater than 100 in both bands and the pixels corresponding to the wake class range from 20 to 70 in the red band and from 50 to 150 in green band. In contrast to these wide distributions, the sea pixels are concentrated at the relatively narrowest spectral ranges of between 20 and 30 in the red band and between 50 and 60 in the green band. The shadow pixels can be discriminated from other classes because of their smallest DN values ranging from 10 to 30 in the red band and from 0 to 30 in the green band, as shown in the lower left of Figure 3(b). This plot shows spatial distributions of the classes in red and green wavelengths. To assess the performance of the classification, the MLC method was applied to all the channels, including blue and near infrared band data.

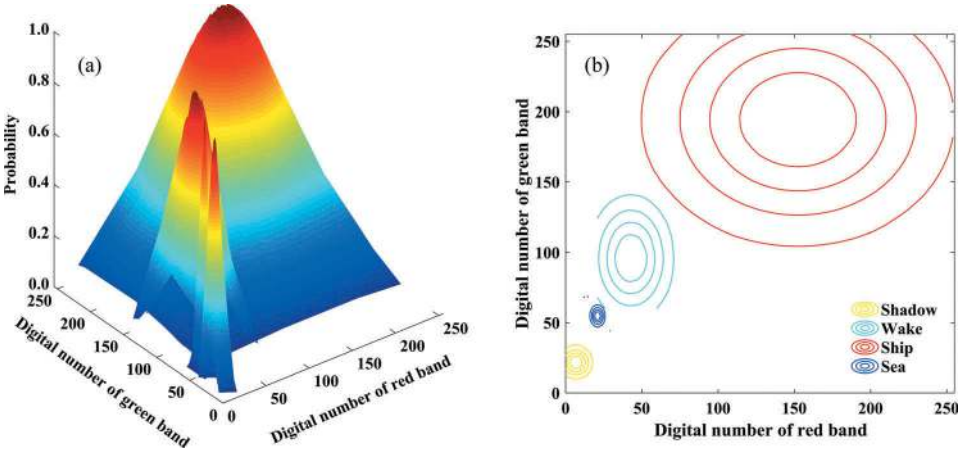

Figure 3. (a) Gaussian probability density function of the four classes (ship, wake, sea, and shadow) and (b) their 2-D distributions, where the elliptic contours represent the probability of each class.

2.4. Ellipse fitting

We used an ellipse fitting method to estimate the ship size because the shape a ship is most similar to an ellipse. To apply the ellipse fitting, the pixel coordinates corresponding to the ship's boundary are required. The locations of the ship periphery were extracted from a 2-dimensional gradient difference of the category values corresponding to the ship pixels and the other surrounding background pixels. The red pixels in Figure 4(a) show the ship pixels detected by MLC method, while the black pixels in Figure 4(b) correspond to the ship boundary obtained from 2-dimensional gradient difference the ship and the

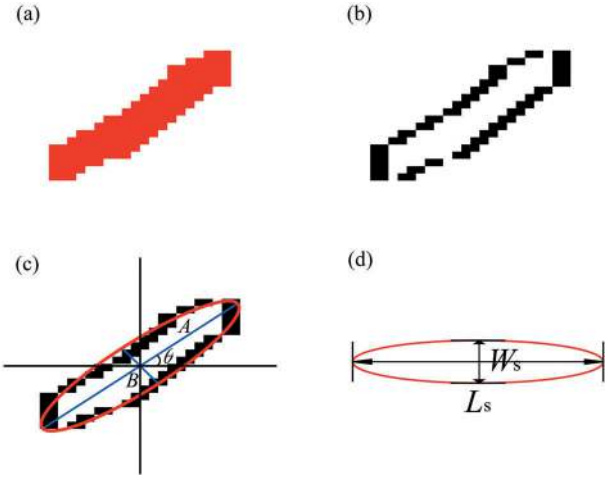

Figure 4. (a) An example of ship pixels detected using the maximum-likelihood classifier method, (b) the spatial distribution of the pixels corresponding to the ship boundary from 2D-gradient difference, (c) an ellipse fitted to the ship edges of (b) where A and B are the major and minor-axis lengths and a tilting angle of θ, and (d) the length (L_S) and width (W_S) of the ship determined from the rotated ellipse of which the major axis aligns to the horizontal line.

background. If the gradient of an image (**S**) including a ship is non-zero, the corresponding pixels are assigned a value of one because they are associated with the ship's boundaries (B_S). If the gradient is zero, the corresponding pixels are assigned a value of zero with *i* and *j* representing the direction of the unit vector. In this study, using gradient difference, we extracted ship boundary pixels from the background of an image. (Equation 1, 2).

$$B_S = \begin{cases} 1\left(|\nabla \mathbf{S}|_{i,j} \neq 0\right) \\ 0\left(|\nabla \mathbf{S}|_{i,j} = 0\right) \end{cases} \tag{1}$$

$$\nabla \mathbf{S}_{i,j} = \sqrt{\left(\frac{\partial \mathbf{S}}{\partial x}\right)_{i,j}^2 + \left(\frac{\partial \mathbf{S}}{\partial y}\right)_{i,j}^2} \tag{2}$$

Overall, all detected ships are not always parallel but are tilted to the horizontal axis. In order to estimate the length and the width of the ship as shown in Figure 4(d), all the elements describing the characteristics of an ellipse, such as major- and minor-axis length, the tilting angle, etc., were derived by performing least-squared fitting of the ellipse equation to the pixel locations of the ship edge. To avoid interference from objects on the ship, we combined two adjacent segments into one if the shortest distance between them was three times as small as the spatial resolution of satellite image. Next, the ellipse was rotated by the tilting angle θ so that its major axis is parallel to the x-axis (Figure 4(d)). The variables *x* and *y* of the general mathematical formula of an ellipse shown in equation (3) are replaced by $x'(= x\cos\theta + y\sin\theta)$ and $y'(= -xsin\theta + ycos\theta)$. Then, the ellipse equation is written in the form of equations (4) and (5). The non-tilting ellipse equation is expressed as Equation (6). The values of *A* and *B* in equation (7) represent the lengths of semi-major and semi-minor axes, and *e* is the eccentricity of the ellipse (Park, Woo, and Ryu 2012).

$$ax^2 + bxy + cy^2 + dx + ey + f = 0 \tag{3}$$

$$\begin{aligned} & x^2\left(a\cos^2\theta - b\cos\theta\sin\theta + c\sin^2\theta\right) \\ & \quad + xy\left(2a\cos\theta\sin\theta + \left(\cos^2\theta - \sin^2\theta\right)b - 2c\cos\theta\sin\theta\right) \\ & \quad + y^2\left(\mathrm{asin}^2\theta + b\cos\theta\sin\theta + c\cos^2\theta\right) + x(d\cos\theta - e\sin\theta) \\ & \quad + y(d\sin\theta e\cos\theta) + f = 0 \end{aligned} \tag{4}$$

$$a_1x^2 + b_1xy + c_1y^2 + d_1x + e_1y + f_1 = 0 \tag{5}$$

$$a_1\left(x + \frac{d_1}{2a_1}\right)^2 + c_1\left(y + \frac{e_1}{2c_1}\right)^2 = -f_1 + \frac{{d_1}^2}{4a_1} + \frac{{e_1}^2}{4c_1} \tag{6}$$

$$A = \sqrt{\left|\frac{-f_1 + \frac{{d_1}^2}{4a_1} + \frac{{e_1}^2}{4c_1}}{2a_1}\right|},\ B = \sqrt{\left|\frac{-f_1 + \frac{{d_1}^2}{4a_1} + \frac{{e_1}^2}{4c_1}}{2c_1}\right|},\ e = \frac{\sqrt{A^2 - B^2}}{A} \tag{7}$$

The parameters of an ellipse constituting the major- and minor-axis lengths, the tilting angle, and the eccentricity of the ship were derived using the ellipse equation with the

ship boundary pixels. The ellipse in Figure 4(c) indicated by the red circle is the result of ellipse fitting of the ship using the least-squared method, where θ is the rotation angle of the ellipse. The length (L_S) and width (W_S) of the ship correspond to the major and minor axes of the ellipse (Figure 4(d)).

3. Results

3.1. Classification of satellite optical image

Figure 5(a) shows an RGB composite image of a representative ship in Figure 2, where the centrally-positioned ship appears brighter than the surrounding dark pixels. The brightness also varies depending on the position of the ship, and relatively dark pixels are distributed in the northwest direction of the ship due to the location of the sun to the southeast, which in the optical images correspond to the shadow of the ship. The height of the shadow tends to increase as it goes to higher latitudes and the height of the ship is high. Figure 5(b) shows the results of the classification into four classes (ship, sea, shadow, and wake) using the MLC method. The red pixels represent the ship class and are located at the central portion with elongated yellow shadow pixels in the northwestern side, which provide a clear contrast to the surrounding sea pixels. There are many other pixels scattered around the sea, and these correspond to the wake pixels (Figure 5(b)).

Figure 6 shows the results of the classification of the KOMPSAT-2 data of the entire study area, including the land, which marked in green. On the left side of image, there are two relatively large anchored ships (S_3 and S_4), near which are three vessels (S_5, S_6, S_7) with considerable wakes located at the southern left corner of the image. In particular, the vessel S_5 is associated with a long wake, reflecting fast movement anticlockwise from the bay to the offshore region. The longer tails of the wakes of vessels S_6 and S_7 at opposite sides of the ships imply that the ships were navigating in different direction, i.e., to the north and south directions. At the right side of the image, there is a ship sailing westward

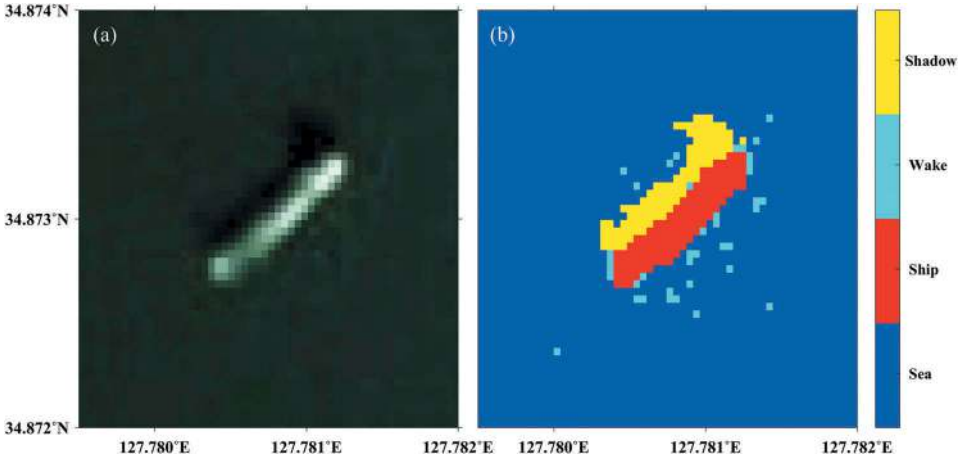

Figure 5. An example of classification: (a) an RGB composite image including a ship and (b) classified results of (a) into four classes of shadow, wake, ship, and sea as the result of applying the maximum likelihood classifier method.

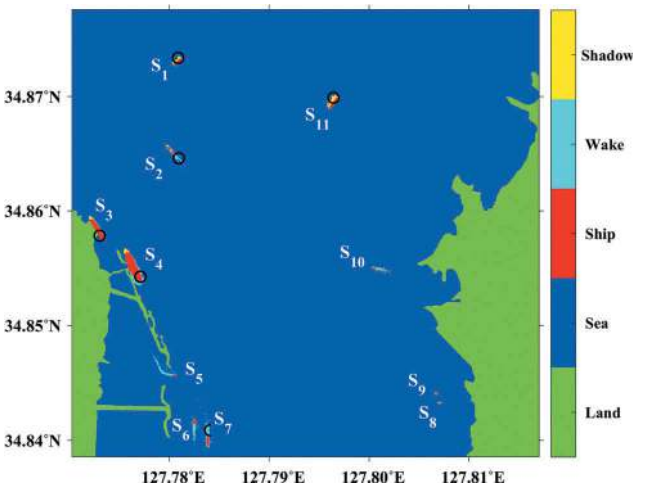

Figure 6. Results of classification of pixels into five classes (shadow, wake, ship, sea, and land) using maximum likelihood classifier method, where the black circles indicate the ship locations (S_1, S_2, S_3, S_4, S_7, and S_{11}) with the AIS data record.

(S_{10}) and other small ships on the lower right corner (S_8, S_9). On the upper left, there is a ship sailing in the northwest direction (S_2) and two other ships with clear shadows (S_1, S_{11}) are seen in the northern direction. A total of eleven ships, either moving or anchored, were properly detected. Aside from the classification results, more information was obtained from the spatial distribution of the wakes and shadows, enabling us to infer, the navigational direction of each ship, at that point in time, based on the spatial distribution of the wake pixels.

3.2. Validation of the ship detection

In order to verify the accuracy of each ship location, we compared the geolocation of the ship from the registered AIS data, which were received within 5 minutes before and after satellite image capture. Only six (S_1, S_2, S_3, S_4, S_7, and S_{11}) out of the eleven ships in Figure 1(e) were identified from the AIS data, but this because only six ships transmitted their positions through the Vessel Monitoring System (VMS) data. The identified vessels are located at the centres of the black circles next to the ships in Figure 6. As shown in Figure 1(f), only five out of the six ships detected transmitted their position through the AIS. In Figure 1(g), four out of the five ships matched AIS data.

Table 2 summarizes the information on space-time locations of the fifteen vessels, records of the locations from AIS data, and observation times and their differences. In the case of S_2, for example, there is a time difference of 13 seconds between the image and the AIS data, with a maximum spatial distance difference of approximately 117 m. Such a large difference may be due to the movement of ship S_3 at a relatively high speed of 9.4 knots, which is confirmed by the detected wake at the rear of the ship. Likewise, the distance difference is large for another moving ship S_7, with 98.5 m difference. In contrast, the stationary ships S_1 and S_{11} have relatively low distance difference values of about 40 m. Among ships V_{1-11}, the maximum space difference is 114.4 m corresponding to V_8,

Table 2. Information on geolocations (latitude and longitude), observation time of satellite image and their AIS data, and distance and time differences between AIS data and KOMPSAT-2/3 image in the southern region of the Korean Peninsula.

		KOMPSAT-2/3				AIS				Difference	
Satellite	Ship	Longitude (°E)	Latitude (°N)	Date	Acquisition Time	Longitude (°E)	Latitude (°N)	Date	Acquisition Time	Distance (m)	Time
KOMPSAT-2	S_1	127.7808	34.8730	12 January 2013	10:25:29	127.7809	34.8734	12 January 2013	10:25:00	40.3	00:00:29
	S_2	127.7801	34.8654	12 January 2013	10:25:29	127.7810	34.8646	12 January 2013	10:25:16	117.3	00:00:13
	S_3	127.7729	34.8584	12 January 2013	10:25:29	127.7731	34.8578	12 January 2013	10:24:54	61.6	00:00:35
	S_4	127.7765	34.8549	12 January 2013	10:25:29	127.7771	34.8542	12 January 2013	10:24:52	86.1	00:00:37
	S_7	127.7839	34.8399	12 January 2013	10:25:29	127.7841	34.8409	12 January 2013	10:25:14	98.5	00:00:15
	S_{11}	127.7965	34.8695	12 January 2013	10:25:29	127.7965	34.8699	12 January 2013	10:25:08	40.7	00:00:21
KOMPSAT-2	V_1	127.7856	34.8751	15 March 2016	02:02:33	127.7856	34.8756	15 March 2016	02:05:07	49.6	00:02:34
	V_2	127.7870	34.8687	15 March 2016	02:02:33	127.7869	34.8689	15 March 2016	02:01:12	23.9	00:01:21
	V_4	127.7962	34.8697	15 March 2016	02:02:33	127.7959	34.8696	15 March 2016	02:03:28	27.1	00:00:55
	V_5	127.7936	34.8736	15 March 2016	02:02:33	127.7935	34.8733	15 March 2016	02:03:24	30.0	00:00:51
	V_6	127.7896	34.8727	15 March 2016	02:02:33	127.7897	34.8729	15 March 2016	02:03:26	20.7	00:00:53
KOMPSAT-3	V_7	127.7550	34.8791	7 September 2014	04:38:33	127.7547	34.8791	7 September 2014	04:38:12	31.3	00:00:21
	V_8	127.7593	34.8773	7 September 2014	04:38:33	127.7584	34.8780	7 September 2014	04:39:02	114.4	00:00:29
	V_{10}	127.7867	34.8796	7 September 2014	04:38:33	127.7690	34.8797	7 September 2014	04:38:55	28.7	00:00:22
	V_{11}	127.7697	34.8807	7 September 2014	04:38:33	127.7705	34.8812	7 September 2014	04:38:45	92.6	00:00:12

and the maximum time difference is 2 minutes and 34 seconds corresponding to V_1. The general distance error between the AIS detected position and that recorded by the Global Position System (GPS) was approximately 100 m (Kim, Park, and Kim 2014).

The geolocations of the fifteen ships registered in the AIS are quite a similar to the locations of the ships in the satellite image. However, a total of seven ships detected through satellite images were not found using AIS data. According to the country's Marine Law, all ferries operating in sea, international shipping vessels weighing more than 300 ton, domestic shipping vessels weighing more than 500 ton, and fishing boats with cargo more than 10 ton must instal the AIS and transmit ship information to a ground station (Ship Safety Act 2009). Smaller vessels less than 10 ton are not obliged to transmit AIS. In light of this, the detected vessel positions can be considered to be in good agreement with the actual vessel positions.

3.3. Characteristics of the classification results

In order to analyse the detailed characteristics of the classified ship and others in its vicinity, all detected ships in Figure 6 were enlarged and compared with the RGB composite images (Figure 7). All objects classified as ships, shadows, wakes, seas, and land classes, are clearly illustrated in the second and fourth columns of Figure 7. The yellow pixels that appear mostly on the upper left of a ship coincide with the shadows of the ships. It follows that the position of the sun determines the direction of the shadows, specifically, the local solar angle at the time of image capture determines the direction of the shadows. On 12 January 2013 at 1:25 UTC, the satellite was located with an azimuth of 145.98° and an altitude of 25.49° at the central position of the satellite image, that is, the sun was located in the southeast direction at the time of imaging. The direction of the shadow of the ship in the satellite image is opposite to the position of the sun, i.e., in the northwest direction (S_1, S_2, S_3, S_4, S_8, S_{11}). The difference in shadow height between S_1 and S_{11} reflects the height of the ship's deck and the wheelhouse. In general, the height of the shadow increases with the rear of the ship because the height of the wheelhouse at the stern is higher than that of the deck at the front.

In the case of a moving ship, it is possible to infer the ship's trajectory based on the wake marked by cyan (S_2, S_5, S_6, S_7, S_{10}). The wake manifests the flow of an object passing over a fluid and generally appears at the back of the ship when the ship moves over the sea. The shape of the wake depends on various factors such as the ship's appearance, propeller, speed, etc. Wakes are generally classified as either turbulent wake or Kelvin wake. A turbulent wake appears linear and in a direction parallel to the ship's direction of movement, while the Kelvin wake appears as two branches in the shape of a V behind the ship, where the maximum angle between the two is 39 (Thomson 1887; Hennings et al. 1999; Dias 2014; Liu and Deng 2018). The two types of wakes also appear in this satellite image. A turbulent wake with a linear shape is shown by ships S_2, S_5, S_6, S_7, and S_{10}. However, ships S_2 and S_{10} also show a v-shaped Kelvin wake. There are some wakes that do not show a specific pattern, and these occur anchor ships or small sized ships (S_1, S_3, S_4, S_8, S_9, S_{11}).

3.4. Ellipse fitting of detected ships and estimation of ship size

The least-squared fitted ellipse was applied to estimate eleven ship sizes detected using the MLC technique. In order to utilize the ellipse equation, arbitrary points constituting

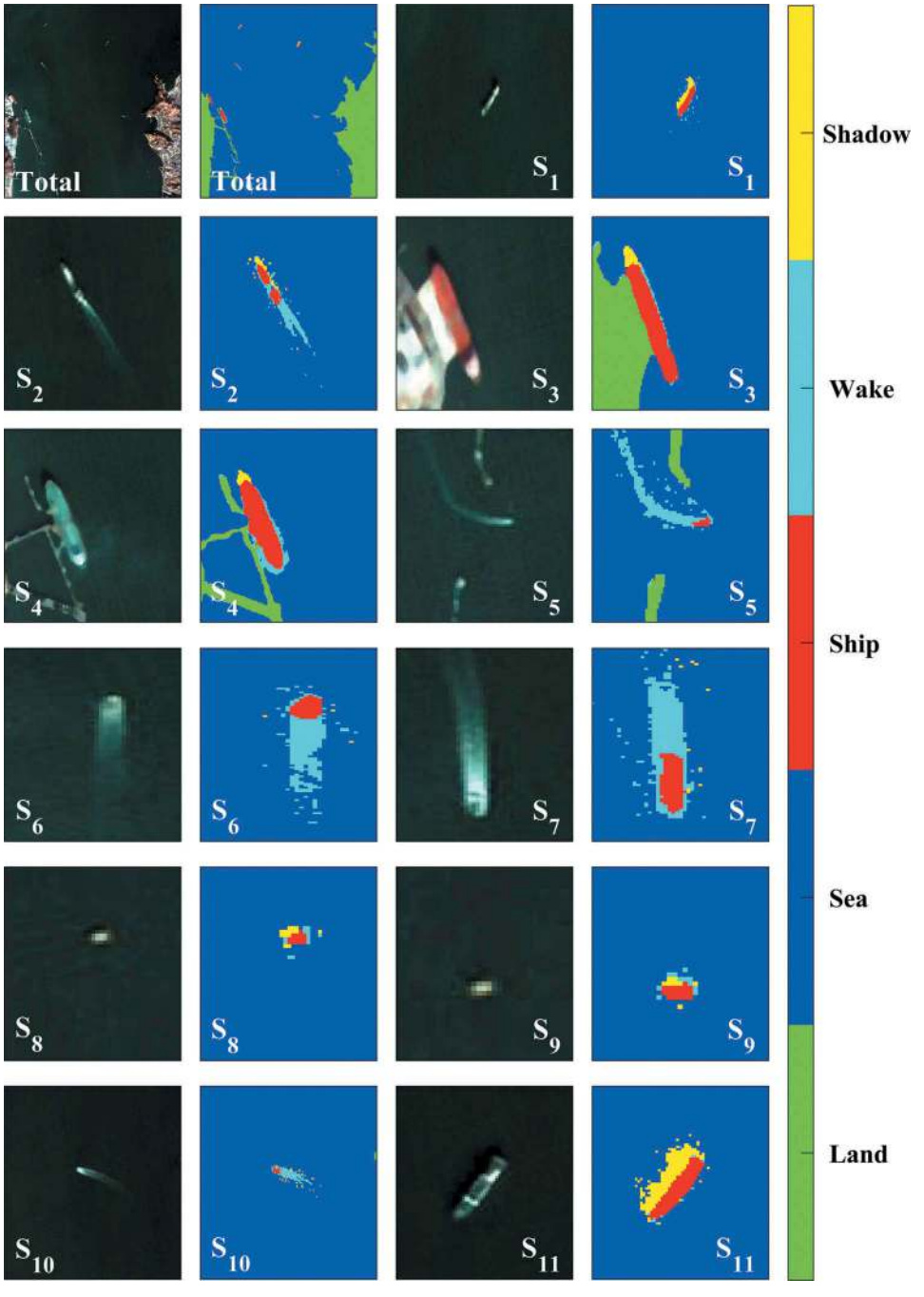

Figure 7. RGB composite images of the ships from S_1 to S_{11} on the first and third columns and the detected ships after applying classification methods to reveal five classes: shadow, wake, ship, sea, and land.

the ellipse are used as boundary pixels of the ship. The pixels representing the ship are assigned a value of one, and the values of the pixels surrounding the ship are substituted with zero; then the 2-dimensional gradients are calculated to separate the boundary

pixels. We then applied the ellipse equations to the selected boundary pixels and extracted the ellipses which are most similar to the actual shape of the ship periphery.

Figure 8 shows the spatial distribution of all the detected ships along with the least-square fitted ellipses. The red and grey colours represent ship pixels and land pixels, respectively, while the ellipses with black contours represent the edge of the ships from the ellipse equation. Most ship pixels are quite consistent with the ellipses except for some overestimation by the ellipses, such as for ships S_3 and S_{11}. Ellipses may overestimate the actual detected ship pixels due to the shape of the boundary pixels at both edges. For example, in the case of a ship with both ends rounded, such as S_1 or S_4, the simulated ellipses are quite similar in size and the shape to those of the actual ships. In contrast, the size of the ellipse of ships S_3 or S_{11} overestimated the actual sizes partly because of straight lines rather than rounded edges at the ends of the ships. We used the same algorithm for the other two satellite images to detect the ship and estimate the size of each ship.

To verify the performance of the aforementioned method, we applied it to two satellite images, as shown in Figure 9. Figure 9(a) shows the ship with ellipses in the KOMPSAT-2 image obtained on 15 March 2016. In total, six ships (V_1 to V_6), coloured in green, were detected. Figure 9(b) shows the ship with ellipses in the KOMPSAT-3 image obtained on 7 September 2014. In total, five ships (V_7 to V_{11}), coloured in blue, were detected. The

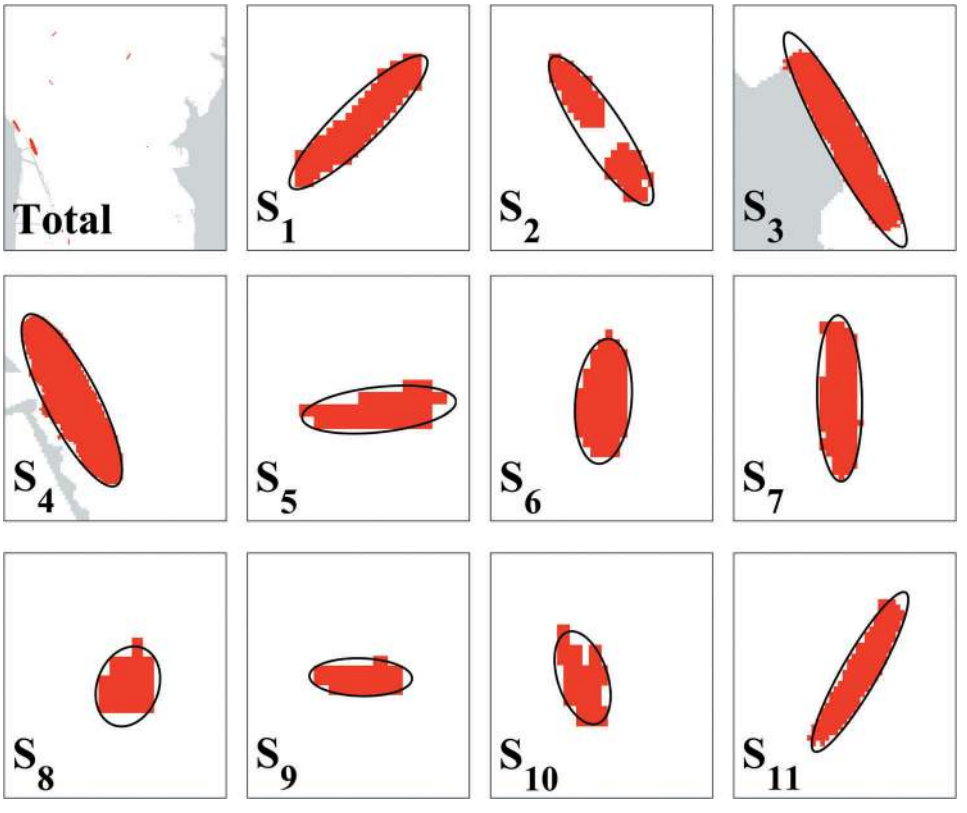

Figure 8. Spatial distribution of the classified pixels corresponding to the ships from S_1 to S_{11}, as marked in red, and least-squared fitted ellipses along the edges of the ships.

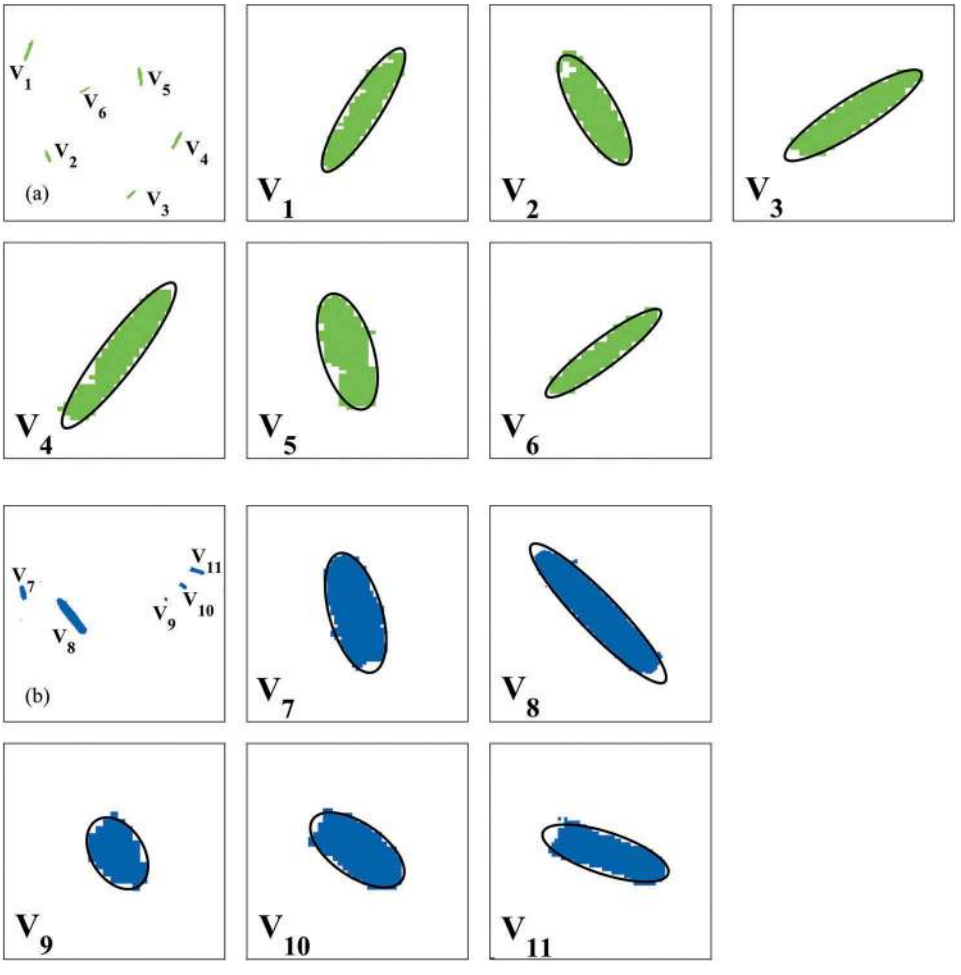

Figure 9. Spatial distribution of the classified pixels corresponding to the ships from V_1 to V_{11}, as marked in green (KOMPSAT-2) and blue (KOMPSAT-3), and least-squared fitted ellipses along the boundary of the ships.

fitted ellipses matched considerably well with the boundaries of the ships. The length of the vessel estimated from the ellipse in Figure 9(a) ranges from 82.4 m to 146.0 m, and the vessel width varies from 14.5 m to 29.1 m. Based on the length of the vessel, the vessels can be classified as V_1, V_4, and V_5, which are relatively large, and V_2, V_3, and V_6, which are smaller. Figure 9(b) shows a wider range of ship lengths from 30.2 m to 352.6 m. Among the vessels between V_1 and V_{11}, V_8 has a length of about 352.6 m and is the largest vessel, which shows the orange deck in the RGB composite image.

Table 3 summarizes the length and width of the ship estimated from the simulated ellipses. Since the detected ships are located in different directions, all the points of the ellipse were rotated by their tilting angles in the horizontal direction parallel to the x-axis and then the lengths of the major and minor axes of the ellipse were calculated. The largest estimated size is for ship S_4, regarded as a large tanker, estimated at 334.9 m in length and 83.4 m in width. On the other hands, the smallest dimensions are for ship S_8,

Table 3. Estimated length and width of each ship from the ellipse fitting procedure.

Ship symbol	Length (m)	Width (m)
S_1	110.1	25.4
S_2	101.7	26.4
S_3	285.9	49.2
S_4	334.9	83.3
S_5	42.0	14.6
S_6	51.3	30.2
S_7	108.3	28.2
S_8	23.7	16.3
S_9	27.8	15.4
S_{10}	36.2	16.4
S_{11}	142.9	30.4
V_1	158.0	27.3
V_2	88.1	25.5
V_3	83.3	19.7
V_4	146.0	25.7
V_5	129.8	29.1
V_6	82.4	14.5
V_7	111.3	41.8
V_8	352.6	68.9
V_9	30.2	20.2
V_{10}	62.0	30.8
V_{11}	115.7	33.0

estimated at 23.7 m in length and 16.3 m in widths, a size corresponding to a small fishing boat. In order to verify the accuracy of ship size estimated by ellipse, we obtained the names and sizes of the ships S_3 and S_4 from Yeosu Gwangyang Port Corporation. The ship S_3 was identified as BEI HAI ZHAN WANG, a Chinese crude oil carrier anchored at the Gwangyang port sappho 1 pier. The length and width of the ship are registered as 244 m and 42 m, respectively, which are 0.85 times and 0.85 times less than the estimated length and width, respectively, from the simulated ellipse. Likewise, the ship S_4 was identified as a NEW RESOURCE crude oil carrier anchored at the Yeosu crude oil pier. The length and width of this ship are registered as 331 m and 60 m, which are 0.98 and 0.72 times less than the respective estimates from the simulated ellipses (Table 4).

3.5. Factors for the overestimation of ship size

3.5.1. Eccentricity

The results reveal that the ellipse fitting approach occasionally overestimates sizes as shown the cases of ships S_3 and S_{11} in Figure 8. To determine the source of errors in estimating ship sizes by ellipse fitting and to investigate potential relationship between estimated and other

Table 4. Information of the ships (S_3 and S_4) including ship name, port name, registered length and width (m). The ratios represent estimated lengths and widths divided by the registered ones, respectively.

Ship symbol	Ship name	Port	Registered length (m)	Registered width (m)	Ratio (length)	Ratio (width)
S_3	BEI HAI ZHAN WANG	Gwangyang port sappho 1 pier	244	42	0.85	0.85
S_4	NEW RESOURCE	Yeosu crude oil pier	331	60	0.98	0.72

parameters representing the shapes of the horizontal cross section of the ships, we collected thirty cross sections of different types of ships of known sizes. All the schematic maps of the cross sections were digitized and converted to 2-dimensional images with spatial coordinates.

Since the sizes and shapes of ships vary according to their purpose, we selected vessel types covering the widest range of the cross-sectional structures as possible. Compared to a fishing ship, cargo ships such as a container ship or a tanker are relatively larger, and the front part of the ship is usually sharper than its rear part. The cross-sectional views of the ships reveal different features in terms of the degree of convexity and asymmetry between the front and the rear parts of the vessels such as aircraft carrier, yachts, and others.

Figure 10 shows the schematic maps of the cross-sections of the ships and their least-squared fitted elliptic shapes marked in red contours for the thirty vessels. Apparently, the ellipses failed to represent the true length of the ships, which may be the source of the overestimation problem. In contrast, the widths of the ships matched comparatively well with the actual widths. Because of the discrepancy between actual and simulated ship lengths, we considered other statistical parameters of the fitted ellipses.

First of all, we considered the eccentricity of the ellipse as one of the primary causes for the error in ship size estimation by ellipse fitting. The eccentricity of an ellipse is expressed as Equation (7) and depends on the ratio of the squares of the semi-major axis length and the semi-minor axis length. The closer the eccentricity is to zero, the more similar the shape of the ellipse is to the circle; the closer the eccentricity is to 1, the closer is the shape to a distorted ellipse. Figure 11(a) shows the errors of ship lengths, ratio of the difference between the estimated and the actual lengths in percentage, and the eccentricity of the ellipse for the cross sections of the thirty vessels. As clearly shown by the scattered errors

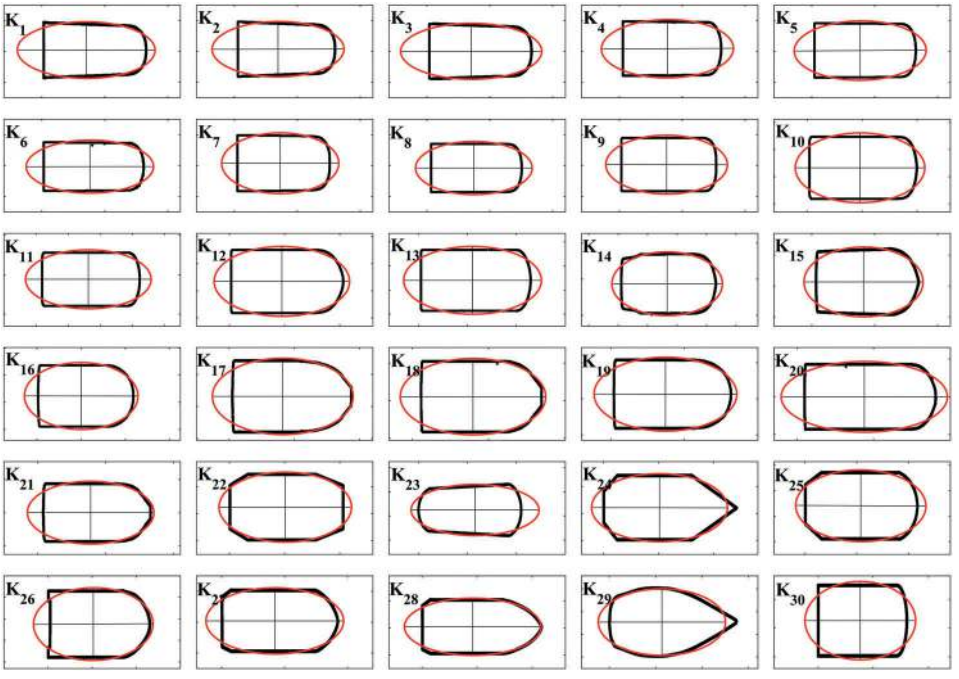

Figure 10. Results of applying an ellipse-fitting method on the periphery of each vessel from K_1 to K_{30}.

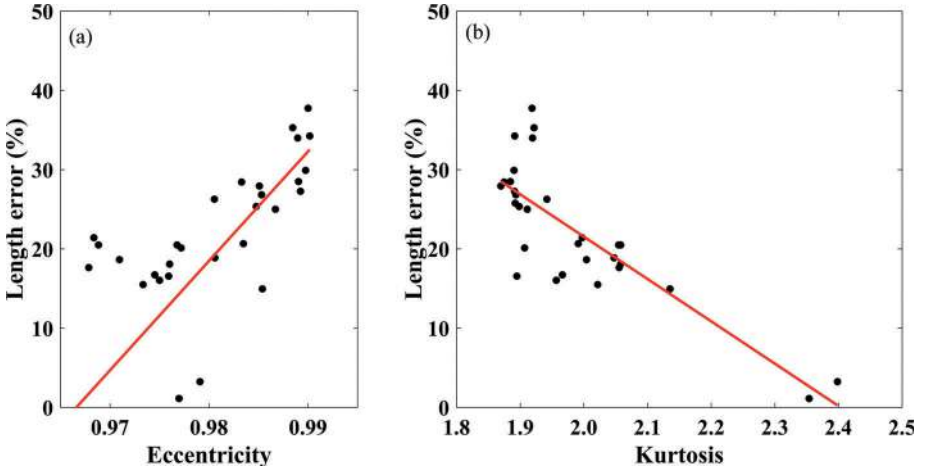

Figure 11. Errors in the estimated lengths of the ships as a function of (a) eccentricity and (b) kurtosis of the ship shape for the fore half of the ship, where the red lines are linear least-squared fits.

and the regression line, the errors of ship lengths have a quadratic relationship to the change in eccentricity. This implies that the errors tended to amplify as the eccentricity was lower as well as higher based on the eccentricity of about 0.97 with the minimum error.

3.5.2. Kurtosis

The shape of the bow of most ship is a pointed triangle, and in the case of a Destroyer, a fast moving warship, the shape is also relatively sharp. Such differences in the cross-sectional shapes of ships suggest that the kurtosis can be an important variable related to the sharpness of the shape of a ship. The cross-section analysis of ship kurtosis shows that the ship length errors tended to decrease as kurtosis of the ship shape increased (Figure 11(b)). When the kurtosis values are less than 2, the length errors reached high values ranging from 16.02% to 37.75%. However, as the kurtosis value increased to about 2.4, the length errors decreased to less than 3.23%. This is associated with the compensation effect due to the differences in the shape of the front and rear ends of the ship. The ellipse fitting tends to underestimated the length of the bow portion of a ship with a high kurtosis, while it is overestimated in the stern portion. Thus, the errors in ship length estimates decrease as the kurtosis increases.

3.6. Adjusted formulation to estimate ship size

Investigation of the errors suggests that the estimation of the ship size can be improved with some parameters of the ship shape in a regression formulation. The correction formula for estimating ship sizes with new length ($L_S{}'$) and width ($W_S{}'$) was derived by considering both the eccentricity of the ellipse and the kurtosis of the detected edges of the ship, as expressed in the following equations:

$$L_S{}' = a_1 L_S + a_2 L_S E + a_3 L_S K + a_4 \tag{8}$$

$$W_S{}' = b_1 W_S + b_2 W_S K + b_3 \tag{9}$$

The equations (8) and (9) are the correction formula for the estimated ship lengths (L_S) and widths (W_S), respectively, where E represents the eccentricity and K represents the kurtosis. The error of in vessel length corresponding to eccentricity is a linear least-squared fit for vessels larger than 0.97, and the error of in vessel length corresponding to kurtosis also shows the first-order regression. We constructed the correction formula to be a linear combination of two variables. The correction formula for ship width is also derived from the linear least-squared fit of the ship width for corresponding to kurtosis. The coefficients corresponding to the two correction formulas are summarized as presented in Table 5.

3.7. Validation of the corrected ship size

Figure 12(a) shows the estimated ship lengths before and after the corrections, which are compared to the actual lengths of the ship cross-sections. The estimated ship lengths derived from the ellipse fitting, marked as black dots, tend to be higher than the actual lengths. This tendency to overestimate was amplified as ship lengths increased, that is, the longer the actual length of the ship, the greater the error, as seen from the large deviations from the expected lengths. For relatively short vessels, the errors tend to decrease, showing discrepancies of less than 5 m. However, when the correction equations are applied, the adjusted lengths, indicated as red dots in Figure 12(a), show good agreement with the actual ship lengths. The RMS error decreased from 7.7 m to 0.7 m after applying the correction procedure (Table 6).

A similar improvement is shown by the estimated ship widths (Figure 12(b)). The estimated ship widths, marked as black dots, tend to be higher than the actual ship

Table 5. Coefficients used for the estimation of ship size in the correction formula (8) and (9).

Ship size	Length				Width		
Coefficient	a_1	a_2	a_3	a_4	b_1	b_2	b_3
Value	6.9468	−6.8203	0.3043	−0.8586	0.6593	0.1163	0.1795

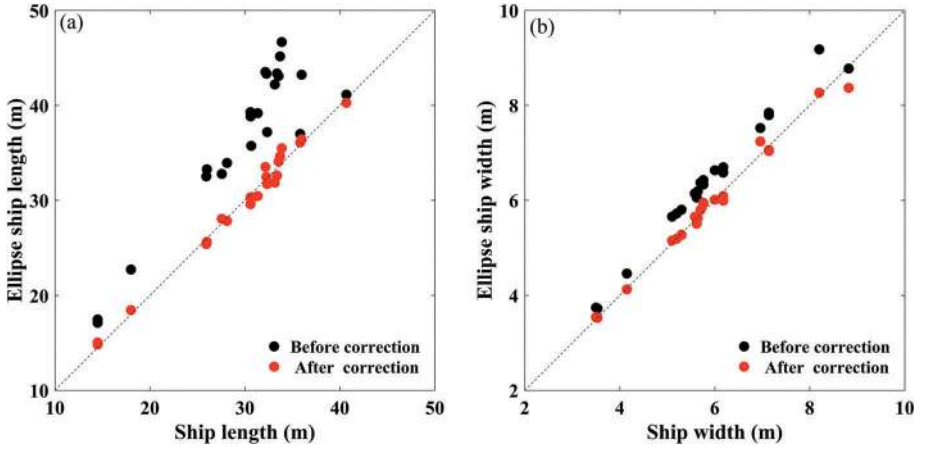

Figure 12. Comparison before and after the correction procedure suggested in this study of (a) the estimated lengths and (b) widths of the ships to the actual dimensions.

Table 6. Comparison of bias and RMS errors for the estimated ship length and width before and after the correction procedure.

	Before		After	
Ship size	Bias	RMSE	Bias	RMSE
Length (m)	7.0	7.7	-1.4×10^{-5}	0.7
Width (m)	0.5	0.5	-0.1×10^{-1}	0.1

widths, although the deviation are much lower (< 1 m) than those for the ship lengths. However, the estimated minor-axis of the ellipse still tend to overestimate the ship length. Thus, the widths were converted to the adjusted widths using the equation (9). As a result, the RMS error also decreased from 0.5 m to 0.1 m as presented in Table 6, which lists the results of the statistical analysis of ship size before and after correction.

3.8. Validation using satellite-observed ships

The accuracies of the ship sizes estimated from satellite images, shown in Figures 8 and 9, was evaluated by applying the correction equation. We extracted the actual ship sizes of ten ships (S_1, S_2, S_3, S_4, S_{11}, V_1, V_2, V_4, V_5, V_8) from AIS data. The AIS data for some ships did not include ship size.

The length of the vessels used for verification ranged from 92 m (V_1) to 331 m (S_4), and the width ranged from 15 m (V_1) to 60 m (S_4). Figure 13 (a) shows the lengths derived from analysis of the satellite images before and after correction. The black dots correspond to the length of the ship estimated by applying the ellipse fitting, that is, the length of the major axis of the ellipse. The red dots indicate the length of the ship after correction by reflecting the eccentricity and kurtosis on the length of the elliptical major axis. The RMS error of the ship length estimated from a simple ellipse was approximately 26.5 m before correction but decreased to approximately 12.1 m after correction. Also, the average bias decreased from approximately 17.6 m to −8.0 m. Figure 13 (b) shows the comparison of the ship width before and after correction. Here too, the black dots indicate that the

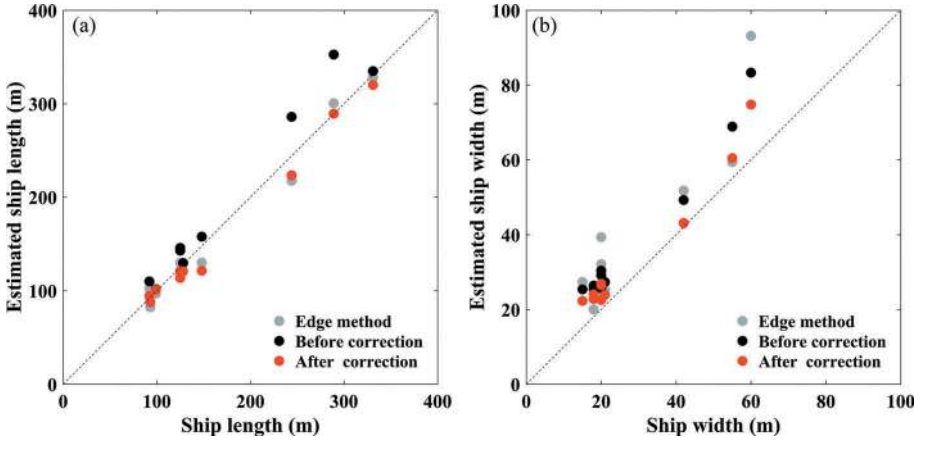

Figure 13. Comparison before and after the correction procedure using satellite images of (a) the estimated lengths and (b) widths of the ships based on AIS data.

ellipse was applied, and the red dots show the results after applying the correction formula. The RMS error of the ship width estimated by simple ellipse fitting was approximately 11.3 m, but after correction, the error decreased to 6.8 m. The average bias decreased from 10.2 m to 5.8 m after correction.

The ship size can be estimated from the longest and shortest distances from the extracted boundary of the ship by rotating the ship pixels by theta. This edge method was applied to the ships and the results were compared with those of the ellipse method. The estimated ship lengths of the edge method, indicated by grey dots, had an RMS error of approximately 12.1 m, which was quite a similar to those for the ellipse method, indicated by red dots. In contrast, the widths estimated by the edge method (grey dots in Figure 13(b)) had remarkably high RMS error, approximately 14.2 m, as compared to that for the ellipse method, 6.8 m. This implies that the ellipse method can be utilized for high accuracy results in the estimation of ship size.

In spite of the application of the correction scheme, however, the length and width estimates of the ship still tended to exceed the actual values. One reason for the discrepancy is the differences between satellite-observed spatial features and the registered lengths and widths of the ships. According to Park et al. (2018), the registered lengths measured at a level several metres below the deck of the ship are always shorter than that of the surface structure of the ship.

4. Summary and conclusion

This study uses the MLC method to detect the ships of various sizes in optical satellite images and to estimate the size of ships as well. A total of twenty-two ships were detected in the KOMPSAT-2/3 image of the study area. To estimate the ship sizes, geolocation information of the pixels at the boundary of the ship was extracted by following the spatially-dominant gradient differences between ship pixels and the surrounding background field and then the least-square fitted ellipse was fitted to the ship boundary pixels. Thereafter, the ship sizes were estimated from the fitted ellipses which are similar to the overall shape of a ship. However, the estimated size of the ship from the ellipse fitting tended to be overestimated. Since ships have varying shapes and sizes, the cross sections of thirty ships of varying types were collected; errors in ship length and width, estimated from the fitted ellipses, were analysed. The primary factors causing the errors are the eccentricity of the ellipse and the kurtosis of the front of the ship. The correction formula developed in this study enabled us to reduce bias and RMS errors of ship size, estimated with ellipses, by a maximum of approximately 54.41%.

The automatic monitoring of the vessels will enable the prompt detection of accidents, which will minimize the impacts of these various types of ship accidents. This study has provided fundamental knowledge and validated methods to enable ship detection and estimation of its size. The methods suggested in this study may be used to monitor ships from satellite images at near-real time. Thus, this study is believed to contribute to both near-real time automation of ship detection and size monitoring for diverse purposes including scientific researches as well as not a few practical uses in marine affairs and management in the future.

Acknowledgements

This research was a part of the project titled 'Development of Management Technology for HNS Accident', funded by the Ministry of Oceans and Fisheries, Korea.

Disclosure statement

No potential conflict of interest was reported by the authors.

Funding

This work was supported by the Ministry of Oceans and Fisheries of Korea.

ORCID

P-Y Foucher http://orcid.org/0000-0002-0435-4573

References

Bi, F., B. Zhu, L. Gao, and M. Bian. 2012. "A Visual Search Inspired Computational Model for Ship Detection in Optical Satellite Images." *IEEE Geoscience and Remote Sensing Letters* 9 (4): 749–753. doi:10.1109/LGRS.2011.2180695.

Corbane, C., F. Marre, and M. Petit. 2008. "Using SPOT-5 HRG Data in Panchromatic Mode for Operational Detection of Small Ships in Tropical Area." *Sensors* 8 (5): 2959–2973. doi:10.3390/s8052959.

Corbane, C., L. Najman, E. Pecoul, L. Demagistri, and M. Petit. 2010. "A Complete Processing Chain for Ship Detection Using Optical Satellite Imagery." *International Journal of Remote Sensing* 31 (22): 5837–5854. doi:10.1080/01431161.2010.512310.

Dias, F. 2014. "Ship Waves and Kelvin." *Journal of Fluid Mechanics* 746: 1–4. doi:10.1017/jfm.2014.69.

ERDAS, L. 1999. *Erdas Field Guide*. Atlanta, GA: Erdas. .

Eriksen, T., G. Høye, B. Narheim, and B. J. Meland. 2006. "Maritime Traffic Monitoring Using a Space-based AIS Receiver." *Acta Astronautica* 58 (10): 537–549. doi:10.1016/j.actaastro.2005.12.016.

Heiselberg, H. 2016. "A Direct and Fast Methodology for Ship Recognition in Sentinel-2 Multispectral Imagery." *Remote Sensing* 8 (12): 1033. doi:10.3390/rs8121033.

Hennings, I., R. Romeiser, W. Alpers, and A. Viola. 1999. "Radar Imaging of Kelvin Arms of Ship Wakes." *International Journal of Remote Sensing* 20 (13): 2519–2543. doi:10.1080/014311699211912.

IALA. 2003. IALA Technical Clarifications on ITU Recommendation ITU-R M.1371-1, Edition 1.4.

Jalkanen, J. P., A. Brink, J. Kalli, H. Pettersson, J. Kukkonen, and T. Stipa. 2009. "A Modelling System for the Exhaust Emissions of Marine Traffic and Its Application in the Baltic Sea Area." *Atmospheric Chemistry and Physics* 9 (23): 9209–9223. doi:10.5194/acp-9-9209-2009.

Kanjir, U. 2019. "Detecting Migrant Vessels in the Mediterranean Sea: Using Sentinel-2 Images to Aid Humanitarian Actions." *Acta Astronautica* 155: 45–50. doi:10.1016/j.actaastro.2018.11.012.

Kanjir, U., H. Greidanus, and K. Oštir. 2018. "Vessel Detection and Classification from Spaceborne Optical Images: A Literature Survey." *Remote Sensing of Environment* 207: 1–26. doi:10.1016/j.rse.2017.12.033.

Kim, D. Y., G. K. Park, and H. Y. Kim. 2014. "A Study on the Ship Information Fusion with AIS and ARPA Radar Using by Blackboard System." *Journal of Korean Institute of Intelligent Systems* 24 (1): 16–21. doi:10.5391/JKIIS.2014.24.1.016.

Kim, H. T., S. Na, and W. H. Ha. 2011. "A Case Study of Marine Accident Investigation and Analysis with Focus on Human Error." *Journal of the Ergonomics Society of Korea* 30 (1): 137–150. doi:10.5143/JESK.2011.30.1.137.

Kim, M., U. H. Yim, S. H. Hong, J. H. Jung, H. W. Choi, J. An, and W. J. Shim. 2010. "Hebei Spirit Oil Spill Monitored on Site by Fluorometric Detection of Residual Oil in Coastal Waters off Taean Korea." *Marine Pollution Bulletin* 60 (3): 383–389. doi:10.1016/j.marpolbul.2009.10.015.

Kim, T. S., K. A. Park, X. Li, M. Lee, S. Hong, S. J. Lyu, and S. Nam. 2015. "Detection of the Hebei Spirit Oil Spill on SAR Imagery and Its Temporal Evolution in a Coastal Region of the Yellow Sea." *Advances in Space Research* 56 (6): 1079–1093. doi:10.1016/j.asr.2015.05.040.

Lee, M. S., K. A. Park, H. R. Lee, J. J. Park, C. K. Kang, and M. Lee. 2016. "Detection and Dispersion of Thick and Film-like Oil Spills in a Coastal Bay Using Satellite Optical Images." *IEEE Journal of Selected Topics in Applied Earth Observations and Remote Sensing* 9 (11): 5139–5150. doi:10.1109/JSTARS.2016.2577597.

Liu, G., Y. Zhang, X. Zheng, X. Sun, K. Fu, and H. Wang. 2014. "A New Method on Inshore Ship Detection in High-resolution Satellite Images Using Shape and Context Information." *IEEE Geoscience and Remote Sensing Letters* 11 (3): 617–621. doi:10.1109/LGRS.2013.2272492.

Liu, Y., and R. Deng. 2018. "Ship Wakes in Optical Images." *Journal of Atmospheric and Oceanic Technology* 35 (8): 1633–1648. doi:10.1175/JTECH-D-18-0021.1.

Mattyus, G. May 21–24 2013. "Near Real-time Automatic Marine Vessel Detection on Optical Satellite Images." International Archives of the Photogrammetry, Remote Sensing and Spatial Information Sciences, Hannover, Germany. doi:10.5194/isprsarchives-XL-1-W1-233-2013

Park, K., J. J. Park, J. C. Jang, J. H. Lee, S. Oh, and M. Lee. 2018. "Multi-Spectral Ship Detection Using Optical, Hyperspectral, and Microwave SAR Remote Sensing Data in Coastal Regions." *Sustainability* 10 (11): 4064. doi:10.3390/su10114064.

Park, K. A., H. J. Woo, and J. H. Ryu. 2012. "Spatial Scales of Mesoscale Eddies from GOCI Chlorophyll-a Concentration Images in the East/Japan Sea." *Ocean Science Journal* 47 (3): 347–358. doi:10.1007/s12601-012-0033-3.

Proia, N., and V. Pagé. 2010. "Characterization of a Bayesian Ship Detection Method in Optical Satellite Images." *IEEE Geoscience and Remote Sensing Letters* 7 (2): 226–230. doi:10.1109/LGRS.2009.2031826.

Qi, S., J. Ma, J. Lin, Y. Li, and J. Tian. 2015. "Unsupervised Ship Detection Based on Saliency and S-HOG Descriptor from Optical Satellite Images." *IEEE Geoscience and Remote Sensing Letters* 12 (7): 1451–1455. doi:10.1109/LGRS.2015.2408355.

Richards, J. A., and X. Jia. 1999. *Remote Sensing Digital Image Analysis: An Introduction, IIIrd Edition*. Heidelberg, Germany: Springer-Verlag.

Scales, W. C., and R. Swanson. 1984. "Air and Sea Rescue via Satellite Systems: Even Experimental Systems Have Helped Survivors of Air and Sea Accidents. Two Different Approaches are Discussed." *IEEE Spectrum* 21 (3): 48–52. doi:10.1109/MSPEC.1984.6370206.

Shi, Z., X. Yu, Z. Jiang, and B. Li. 2014. "Ship Detection in High-resolution Optical Imagery Based on Anomaly Detector and Local Shape Feature." *IEEE Transactions on Geoscience and Remote Sensing* 52 (8): 4511–4523. doi:10.1109/TGRS.2013.2282355.

Shin, S. 2013. "A Study on the Countermeasures against Illegal Fishing by Chinese Boats." *Maritime Law Review* 25 (3): 217–248.

Ship Safety Act. 2009. Korea Ministry of Government Legislation.

Tang, J., C. Deng, G. B. Huang, and B. Zhao. 2015. "Compressed-domain Ship Detection on Spaceborne Optical Image Using Deep Neural Network and Extreme Learning Machine." *IEEE Transactions on Geoscience and Remote Sensing* 53 (3): 1174–1185. doi:10.1109/TGRS.2014.2335751.

Thomson, W. 1887. "On the Waves Produced by a Single Impulse in Water of Any Depth, or in a Dispersive Medium." *Proceedings of the Royal Society of London*, 42: 80–83. doi:10.1098/rspl.1887.0017

Wu, G., J. de Leeuw, A. K. Skidmore, Y. Liu, and H. H. Prins. 2009. "Performance of Landsat TM in Ship Detection in Turbid Waters." *International Journal of Applied Earth Observation and Geoinformation* 11 (1): 54–61. doi:10.1016/j.jag.2008.07.001.

Xu, J., X. Sun, D. Zhang, and K. Fu. 2014. "Automatic Detection of Inshore Ships in High-resolution Remote Sensing Images Using Robust Invariant Generalized Hough Transform." *IEEE Geoscience and Remote Sensing Letters* 11 (12): 2070–2074. doi:10.1109/LGRS.2014.2319082.

Yang, G., B. Li, S. Ji, F. Gao, and Q. Xu. 2014. "Ship Detection from Optical Satellite Images Based on Sea Surface Analysis." *IEEE Geoscience and Remote Sensing Letters* 11 (3): 641–645. doi:10.1109/LGRS.2013.2273552.

Yao, Y., Z. Jiang, H. Zhang, M. Wang, and G. Meng. March 2 2016. "Ship Detection in Panchromatic Images: A New Method and Its DSP Implementation." International Society for Optics and Photonics, Xiamen, China.

Zhang, W., F. Goerlandt, J. Montewka, and P. Kujala. 2015. "A Method for Detecting Possible near Miss Ship Collisions from AIS Data." *Ocean Engineering* 107: 60–69. doi:10.1016/j.oceaneng.2015.07.046.

Zhao, Z., K. Ji, X. Xing, H. Zou, and S. Zhou. 2014. "Ship Surveillance by Integration of Space-borne SAR and AIS–Review of Current Research." *The Journal of Navigation* 67 (1): 177–189. doi:10.1017/S0373463313000659.

Zhu, C., H. Zhou, R. Wang, and J. Guo. 2010. "A Novel Hierarchical Method of Ship Detection from Spaceborne Optical Image Based on Shape and Texture Features." *IEEE Transactions on Geoscience and Remote Sensing* 48 (9): 3446–3456. doi:10.1109/TGRS.2010.2046330.